ARTICLE

Enhancing Cycling Stability of Tungsten Oxide Supercapacitor Electrodes via a Boron Cluster-Based Molecular Cross-Linking Approach

Dahee Jung,[*‡a,b] Mit Muni,[‡a] Gustavo Marin,[a] Roshini Ramachandran,[a] Maher F. El-Kady,[a,b] Tanya Balandin,[a] Richard B. Kaner[*a,b,c] and Alexander M. Spokoyny[*a,b]

We report our discovery of utilizing perhydroxylated dodecaborate clusters ($[B_{12}(OH)_{12}]^{2-}$) as a molecular cross-linker to generate a hybrid tungsten oxide material. The reaction of $[B_{12}(OH)_{12}]^{2-}$ with WCl_6, followed by subsequent annealing of the product at 500 °C in air successfully produces a tungsten oxide material cross-linked with B_{12}-based clusters. The comprehensive structural study of the produced hybrid material confirms a cross-linked network of intact boron-rich clusters and tungsten oxides. We further demonstrate how these robust B_{12}-based clusters in the resulting hybrid tungsten oxide material can effectively preserve the specific capacitance up to 4000 cycles and reduce the charge transfer resistance as well as the response time compared to that of pristine tungsten oxide. Ultimately, this work highlights a promising capability of boron-rich cluster in the hybrid metal oxide to obtain fast and stable supercapacitors with high capacitance.

Introduction

Supercapacitors are a class of energy storage devices found commonly in hybrid electric vehicles, camera components and used as backup power systems.[1] One class of supercapacitors, called electric double layer capacitors (EDLCs), are a popular option for commercial applications. In EDLCs, electrolyte ions are adsorbed onto the electrode/electrolyte interface of high-surface area carbon and charge is stored solely via this electrostatic double layer. Due to this charge storage process, the structural integrity of the electrode is maintained resulting in high power densities and cycle lifetimes of over one million cycles.[2] One major drawback of these devices is their low energy density, which limits their use in many applications. To improve the energy density of supercapacitors, many transition metal oxides such as V_2O_5, $Ni(OH)_2$, Co_3O_4, RuO_2, MnO_2 and WO_3 have been investigated.[3-8] Unlike carbon-based materials, transition metal oxides undergo Faradaic reactions that facilitate charge storage. Due to accessible redox states, transition metal oxides have much higher energy densities, but most suffer from low conductivity and poor cycling stability.[9] In particular, tungsten oxide has been suggested as a potential alternative for supercapacitor electrode materials due to its redox active properties.[8-10] Recent efforts have focused on improving tungsten oxide containing supercapacitors including their electrochemical performance, rate, and cycling stability in order to improve this material for energy storage applications.[8,10-12]

Over the past several years, different strategies have been employed to improve the performance of metal oxide-based supercapacitors. One strategy is to switch from bulk materials to nanomaterials (**Fig. 1a**).[7] Due to their high surface area, more redox active sites are available on the nanostructured metal oxides; however, the transfer of electrons through these materials is still not as efficient as desired. The vast majority of metal oxide materials for energy storage applications have focused on using conductive supports for metal oxide nanoparticles to facilitate efficient electron transfer (**Fig. 1b**).[13-16] 0-D, 1-D, 2-D and 3-D carbon-based materials such as carbon nanodots, carbon nanotubes, graphene and carbon aerogels are often used due to their high conductivity, large surface area and versatility.[13-16] Conducting polymers such as polypyrrole and polyaniline are also used, however, they too suffer from limited cyclability (**Fig. 1c**).[17] Recently, a covalent cross-linking approach has been introduced to manipulate the properties of metal oxides utilizing a perhydroxylated dodecaborate cluster ($[B_{12}(OH)_{12}]^{2-}$, referred to as **I**) as a molecular cross-linker.[18]

In this approach, the B_{12}-based cluster, **I**, was used as a polyol precursor in a manner similar to how organic alcohols are used in the sol-gel process.[19] Our previous report demonstrated that the reaction of **I** with titanium tetraisopropoxide ($Ti(O^iPr)_4$), followed by annealing at 500 °C, led to the formation of B-O-Ti linkages in the resulting hybrid materials stemming from intact boron clusters.[17] It should be noted that in contrast to organic molecules, which normally completely decompose during annealing at high temperature (~500 °C) in air,[20] the inorganic
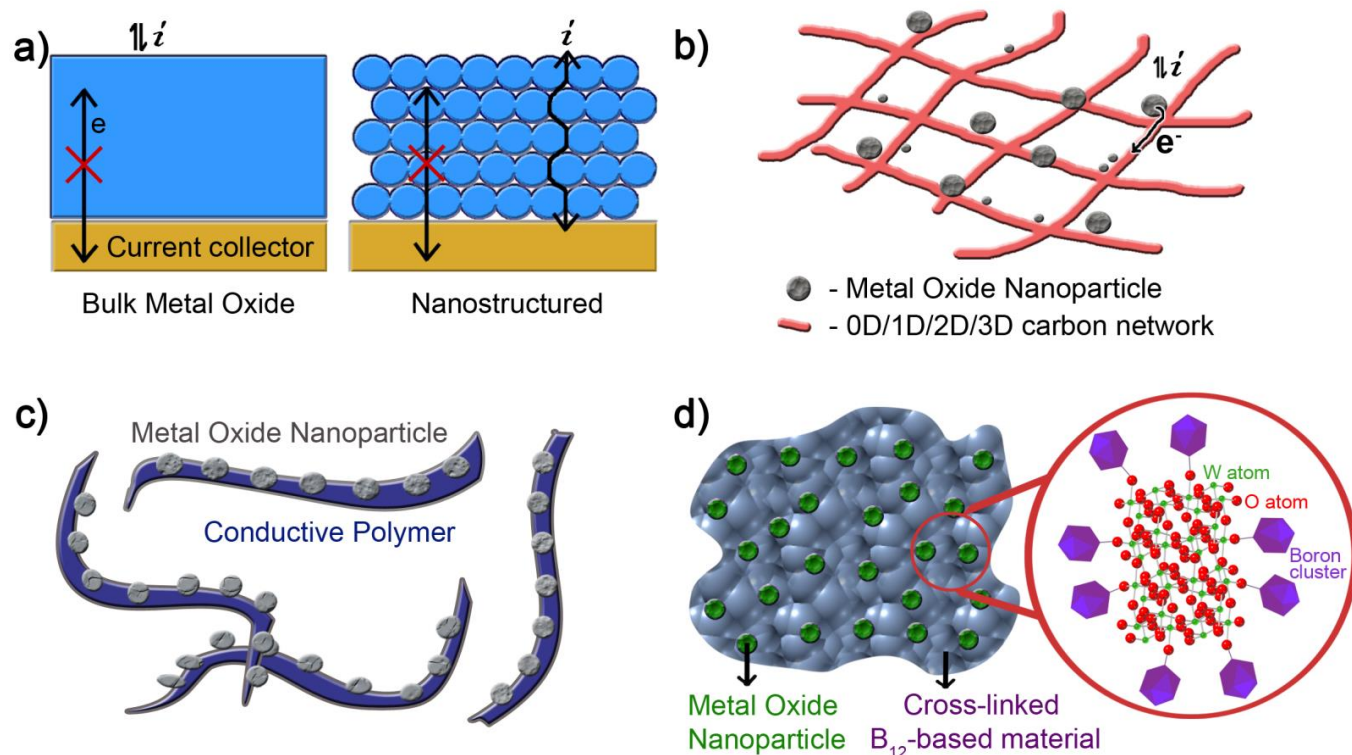
Fig. 1 Overview of existing strategies to improve the performance of metal oxide-based supercapacitors. (a) nanostructuring of bulk metal oxides. (b) carbon composites, and (c) conducting polymer composite materials. (d) Molecularly cross-linked hybrid metal oxides.

polyol, **I**, remained partially intact allowing it to form a hybrid cross-linked material. The resulting boron-rich hybrid TiO_2 material subsequently conferred unique electrochemical properties to the parent metal oxide. Specifically, cross-linking **I** to the network of TiO_2 resulted in increased specific capacitance and a faster electron transfer rate in the resulting hybrid material compared to pristine TiO_2. Furthermore, the robust molecular scaffold of **I** due to the high degree of electron delocalization provided outstanding thermal and chemical stabilities.[21,22]

In this study, we apply the developed cross-linking approach to a tungsten-based system in order to produce a boron-rich hybrid tungsten oxide material (**Fig. 1d**). Considering that the molecular cross-linking approach promotes a synergy of the functionalities of the material and cross-linker,[23] we executed this strategy with tungsten oxide aiming to create a supercapacitor electrode. Our work shows that the incorporation of the robust molecular cross-linker, **I**, into the tungsten oxide network generates a chemically stable hybrid material, which significantly enhances the long-term cycling stability in the electrochemical reactions. We further demonstrate that the charge transfer resistance and the response time are significantly reduced in the resulting boron-rich hybrid material in comparison to that of pristine tungsten oxide.

Experimental

Materials: Deuterated solvents were purchased from Cambridge Isotope Laboratories and used as received. The

following chemicals were purchased from commercial vendors: tungsten hexachloride (Acrosorganics). [N^nBu_4]$^+$ salts of [$B_{12}(OH)_{12}$]$^{2-}$ were synthesized by previously reported methods.[24]

Synthesis of Material 1: The preparation of the microwave reaction was carried out in an inert atmosphere dry-box. In a 10 ml glass microwave vial, WCl_6 (24 mg, 0.0611 mmol) in acetonitrile (1 ml) was added to a stirring suspension of [N^nBu_4]$_2$[$B_{12}(OH)_{12}$] (50 mg, 0.0611 mmol) in acetonitrile (0.5 ml). The reaction vial was sealed with a PTFE/silicone cap and then brought outside of the dry-box. The mixture was heated at 120 °C with stirring in the microwave for 30 min. The red-orange gel reaction mixture was washed with ethanol three times and dried at 80 °C for 2 h in air. The dried powder was annealed by heating from room temperature to 500 °C in air at a rate of 10 °C/min and holding at 500 °C for 3 h. Then, the furnace was cooled to room temperature at a rate of 1 °C/min.

Synthesis of Material 2. In a 10 ml glass microwave vial, WCl_6 (290 mg, 0.733 mmol) in acetonitrile (2 ml) was added to a stirring suspension of [N^nBu_4]$_2$[$B_{12}(OH)_{12}$] (50 mg, 0.0611 mmol) in acetonitrile (0.5 ml). The rest of the procedure is the same as that used for material **1**.

Synthesis of monoclinic tungsten oxides: In a 10 ml glass microwave vial, WCl_6 (200 mg, 0.504 mmol) was added into ethanol (3 ml). The vial was sealed and transferred to a benchtop microwave reactor. The mixture was heated at 120 °C with stirring in the microwave for 30 min. After the reaction, the

product was washed with ethanol 3 times and dried at 80 °C in air for 2 h. The dried powder was annealed in the same way as materials **1** and **2**.

Characterization Methods and Instrumentation:

Powder X-ray diffraction (PXRD) patterns were collected on a Panalytical X'Pert Pro X-ray Powder Diffractometer with Cu-Kα radiation. Diffraction spectra were collected from a 2θ angle of 10 to 80 degree with a step size of 0.04 degree at a rate of 1 degree/min. High-resolution transmission electron microscopy (HRTEM) was performed using a FEI Titan S/TEM operated at 300 kV. X-ray photoelectron spectroscopy (XPS) spectra were obtained on an AXIS Ultra DLD instrument (Kratos Analytical Inc., Chestnut Ridge, NY, USA). All XPS spectra were obtained using a monochromatic Al Kα X-ray source (12 mA for both survey and high-resolution scans, 15 kV) with a 300 x 700 nm oval spot size. The pressure of analyzer chamber was maintained below 1×10^{-8} Torr during the measurement. Spectra were collected with 160 eV pass energy for survey spectra and 20 eV for high-resolution spectra of C 1s, O 1s, B 1s, and W 4f. All XPS peaks were charge referenced to the adventitious carbon 1s signal at 284.6 eV. Infrared (IR) was performed using a PerkinElmer Spectrum One instrument equipped with a universal ATR assembly. Scanning electron microscopy (SEM) was undertaken using a field-emission SEM (JEOL JSM 6700F). ^{11}B solution NMR spectra were recorded in acetonitrile on AV 400 spectrometers in ambient conditions. [11]B solid-state magic angle spinning (MAS) nuclear magnetic resonance (NMR) spectra were acquired on a 600 MHz (14.1 T) Bruker AVANCE III HD spectrometer using a 3.2 mm HXY MAS probe. The MAS frequency used was 20 kHz for [11]B. The [11]B background signal from the MAS probe was suppressed using the EASY sequence.[25] The [11]B chemical shift was indirectly referenced to $BF_3O(CH_2CH_3)_2$ in $CDCl_3$ by using $Cs_2[B_{12}(OH)_{12}]$ (δ=-17.7 ppm).[18] The RF field for the [11]B central transition selective pulse was 66 kHz. N_2 isotherms were obtained at 77 K on a micromeritics Tristar after activation at 120 °C under vacuum overnight.

Electrochemical Measurements

Electrochemical measurements were conducted using a Biologic VMP3 electrochemical workstation (VMP3b-10, Science Instruments). All electrochemical measurements were conducted using a three-electrode set-up that utilized an Ag/AgCl reference electrode (Basi Inc.) and a platinum foil counter electrode (Fisher Scientific) in 1.0 M H_2SO_4. Working electrodes were made by combining the active material (m-WO_3, Material **1** or Material **2**) with 10 wt% PVDF binder and 10 wt% carbon black in N-methylpyrrolidinone. The solution was mixed using a homogenizer and then drop-cast onto a graphite current collector with an area of 1 cm². A method developed by Nicholson was used to determine the heterogeneous electron transfer rate constant, k^0, using the equation:

$$\varphi = \frac{\left(D_0/D_R\right)^{\alpha/2} k^0}{\left(\pi D_0 vF/RT\right)^{\frac{1}{2}}} \quad (1)$$

where φ is a dimensionless kinetic parameter related to the peak separation (ΔE_p). The other variables represent the diffusion coefficients of the oxidized (D_0) and reduced (D_R) species, transfer coefficient (α), heterogeneous electron rate transfer constant (k^0), scan rate (v), Faraday constant (F), ideal gas constant (R) and temperature (T). The redox system used to determine k^0 was 2.0 mM $K_3[Fe(CN)_6]$ dissolved in a 0.10 M KCl solution. The diffusion coefficients for the oxidized and reduced forms of $[Fe(CN)_6]^{3-/4-}$ in 0.10 M KCl are similar, therefore $(D_0/D_R)^{\alpha/2} \approx 1$.[26, 27]

Gravimetric capacitance (C_g)(F/g)) was calculated from the CV curve of the cathodic scan of each material, using the formula:

$$C_g = \frac{\int_{V_i}^{V_f} i\,(V)\,dV}{m\,v\,(V_f - V_i)} \quad (2)$$

where i is the current response, V_f and V_i are the final and initial voltage, v is the scan rate, and m is the mass of the electrode. The real and imaginary capacitance was calculated from impedance data using the formulas:

$$C'(\omega) = \frac{-Z''(\omega)}{\omega\,|Z(\omega)|^2} \quad (3)$$

$$C''(\omega) = \frac{Z'(\omega)}{\omega\,|Z(\omega)|^2} \quad (4)$$

where $C'(\omega)$ is the real capacitance and $C''(\omega)$ is the imaginary capacitance. Other variables include the imaginary impedance ($-Z''(\omega)$), real impedance ($-Z'(\omega)$) and the complex impedance ($|Z(\omega)|^2$) where $|Z(\omega)|^2 = Z'^2 + Z''^2$.[28]

Results and discussion

Similar to our previous work with group 4 transition metal oxides, we expected the B-OH moieties in **I** to be able to react with WCl_6, forming B-O-W linkages to produce a cross-linked tungsten oxide hybrid material (**Fig. 2a**).[18,21,29-31] To test this hypothesis, **I** was reacted with one equivalent of WCl_6 (1 tungsten metal equivalence per B_{12}-based cluster) in acetonitrile at 120 °C using a benchtop microwave reactor. After 30 min, the reaction mixture produced a red-orange gel (**Fig. S1**). The supernatant liquid from the reaction was subject to [11]B solution nuclear magnetic resonance (NMR) spectroscopy to detect unreacted B_{12}-based clusters. The ^{11}B solution NMR spectrum of the supernatant liquid showed an absence of any boron containing species, suggesting that the majority of the boron cluster precursor is contained in the gel-based material (**Fig. S2**). The solid residue from the reaction was dried and annealed to form a crystalline black material (referred to herein as material **1**) (**Fig. 2 inset**). The structure of the resulting solid material was elucidated by powder X-ray diffraction (PXRD); which showed that material **1** possesses a crystalline structure that can be indexed to the monoclinic phase of WO_3 (**Fig. 2b**).[32-]
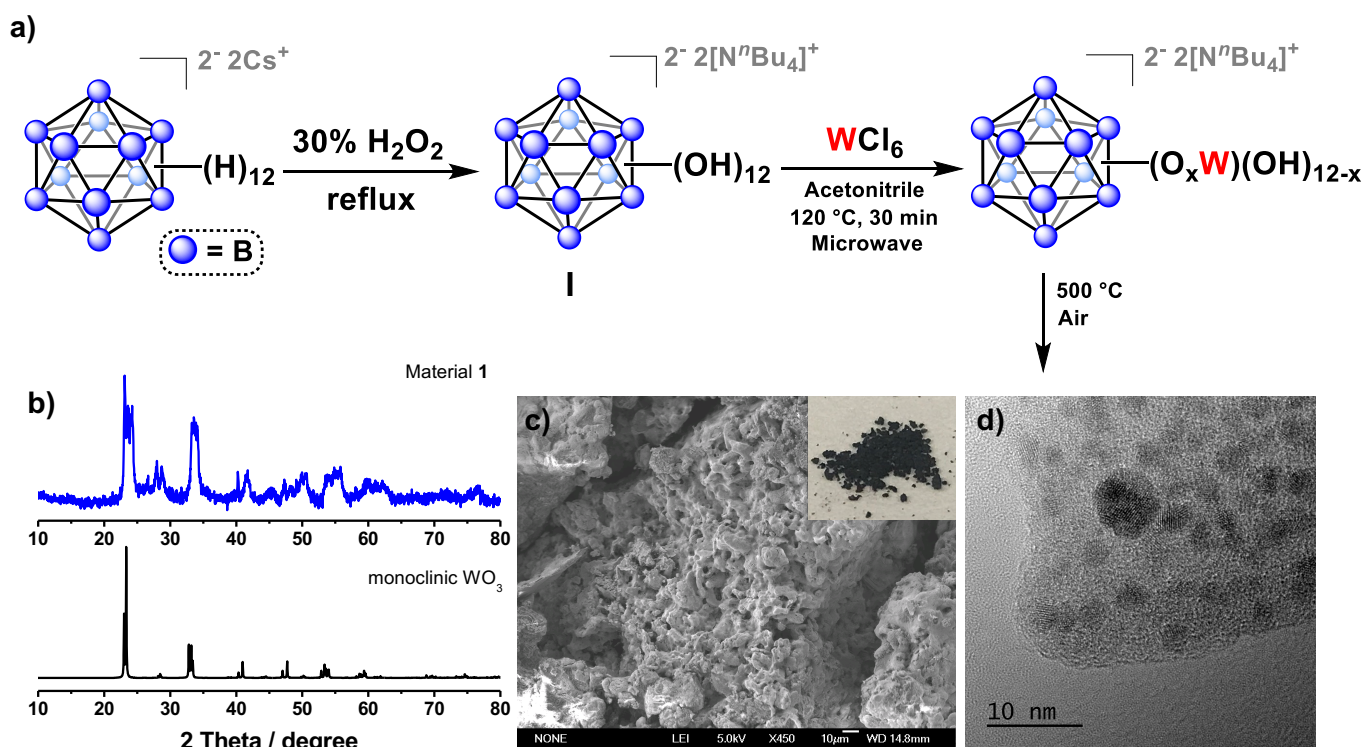
Fig. 2 (a) A synthetic route to produce material **1**. (b) powder X-ray diffraction (PXRD) patterns of material **1** and monoclinic WO$_3$. (c) scanning electron microscopy (SEM), (d) transmission electron microscopy (TEM) image of material **1**.

[34] The broad peaks in the PXRD pattern can be attributed to the small crystal size of WO$_3$ (< 10 nm) in material **1.** The surface morphology and elemental composition of material **1** were obtained using scanning electron microscopy (SEM) and energy dispersive X-ray spectroscopy (EDS). The SEM images of **1** suggested the likely formation of a porous structure at the surface upon cross-linking boron-rich clusters to the tungsten oxide network (**Fig. 2c**). Moreover, the EDS elemental analysis showed that material **1** consisted of boron, oxygen, tungsten and carbon with 12.2, 73.9, 4.6 and 7.5 %, respectively (**Fig. S3**). Noticeably, no chlorine was detected, providing additional support that the B-O-W linkage is possibly formed through the reaction between **I** and WCl$_6$ with the concomitant formation of HCl. Furthermore, the Fourier transform infrared (FT-IR) spectrum of material **1** displayed a broad peak below the 1000 cm^{-1} region which is characteristic of W-O stretching vibrations

(**Fig. S4**).[35] High-resolution TEM (HRTEM) images of material **1** highlighted the morphology of nanocrystalline WO$_3$ particles with additional amorphous material, which can be attributed to intact boron cluster units and boron oxide (**Fig. 2d**). X-ray photoelectron spectroscopy (XPS) measurements were performed to investigate the surface environment of material **1**. The boron 1s region exhibited two components at 189.8 and 194.1 eV, corresponding to the presence of intact dodecaborate clusters as well as boron oxide and borates (**Fig. 3a**). The W 4f XPS spectrum consisted of two peaks of 4f$_{7/2}$ and 4f$_{5/2}$ at 36.2 and 38.3 eV, respectively which are well-matched to those of W(VI) trioxides (**Fig. 3b**). The O 1s region showed multiple components at 530.8, 531.4, and 533.1 eV, which can be assigned to O-W, O-C, and O-B, respectively (**Fig. 3c**).[36] The atomic compositions obtained from XPS analyses demonstrated that boron (21%) and oxygen (51%) are dominant while there is
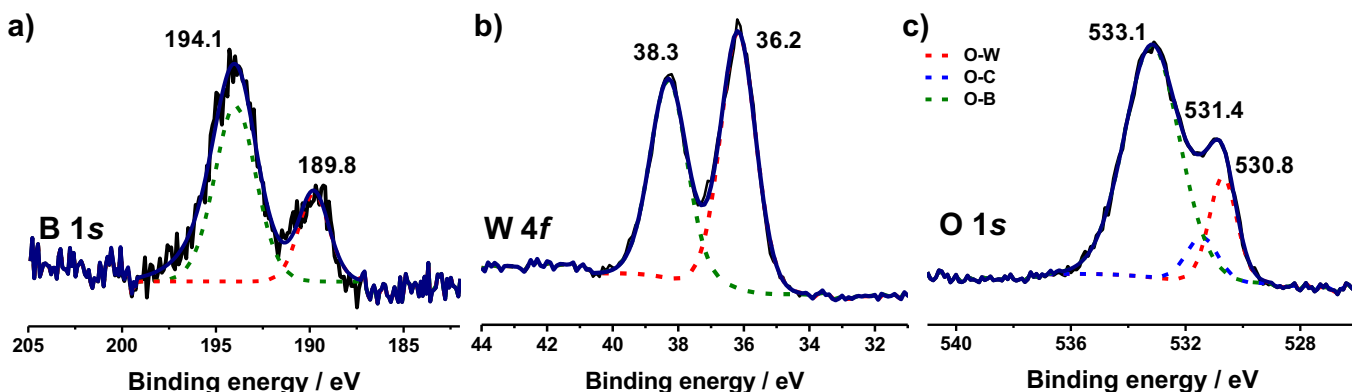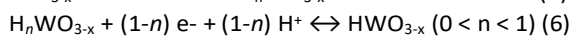

Fig. 3 X-ray photoelectron spectroscopy (XPS) spectra of material **1**. (a) B 1*s*, (b) W 4*f*, (c) O 1*s* region.

only 5% of tungsten at the surface (**Table S1**). This result is consistent with the TEM image of material **1** which suggests that the tungsten oxide nanoparticles are embedded in the layer consisting of a cross-linked network of intact B_{12}-based clusters as well as some boron oxides.

The presence of intact B_{12}-based clusters in material **1** was directly verified using solid-state ^{11}B NMR spectroscopy, which can provide the local environment of [11]B atoms in the material. The 1D single-pulse [11]B magic angle spinning (MAS) SSNMR of material **1** showed three distinct features. The peak at -15.7 ppm was assigned to the sub-surface dodecaborate clusters which are directly bound to the tungsten oxide network based on the signal from a reference material containing $Cs_2[B_{12}(OH)_{12}]$ (**Fig. S5 and S6**). Two additional signals at 0.7 and 12.9 ppm can be attributed to the partially intact B_{12}-based clusters at the surface and to boron oxide or borates, respectively.[18,37] These observations are consistent with our previous work on Ti-based system which showed three distinct signals at -16, 2, and 17 ppm in the ^{11}B MAS NMR that can be attributed to the intact B_{12}-based clusters, partially intact clusters at the particle surface and boron oxides and borates in the material, respectively.[18] The combined structural and morphological characterizations of material **1** validate that the hybrid tungsten oxide material is composed of nano-crystalline monoclinic WO_3 particles cross-linked with molecular boron clusters, **I**, as represented in **Figure 1d**.

Many metal oxide-based supercapacitors provide high specific capacitance. Although promising values ranging from 232 – 510 F/g for various morphologies of WO_3 have been achieved, these high capacitances are typically limited to very slow scan rates.[38,39] The charge storage mechanism of WO_3 can be rationalized as two stages of proton intercalation reaction accompanied by the change in oxidation state of W^{6+} to W^{5+}:[40]

$$WO_{3-x} + nH^+ + ne^- \leftrightarrow H_nWO_{3-x} \qquad (5)$$
$$H_nWO_{3-x} + (1\text{-}n)\, e^- + (1\text{-}n)\, H^+ \leftrightarrow HWO_{3-x}\ (0 < n < 1)\ (6)$$

To determine the capacitance of material **1**, we conducted cyclic voltammetry at varying scan rates with a voltage window from -0.5 V to 0.6 V (**Fig. 4a**). As a control experiment, we also prepared monoclinic tungsten oxide (m-WO_3) and another hybrid tungsten oxide material using a different ratio of B_{12}-based cluster to tungsten (12-tungsten metal equivalences per B_{12}-based cluster, referred to material **2**) to provide benchmark values (**Fig. S7-12**). For pristine m-WO_3, the maximum capacitance value at 1 mV/s was determined to be 283 F/g, which is similar to previously reported values.[39] For materials **1** and **2**, the specific capacitances were determined to be 31 F/g
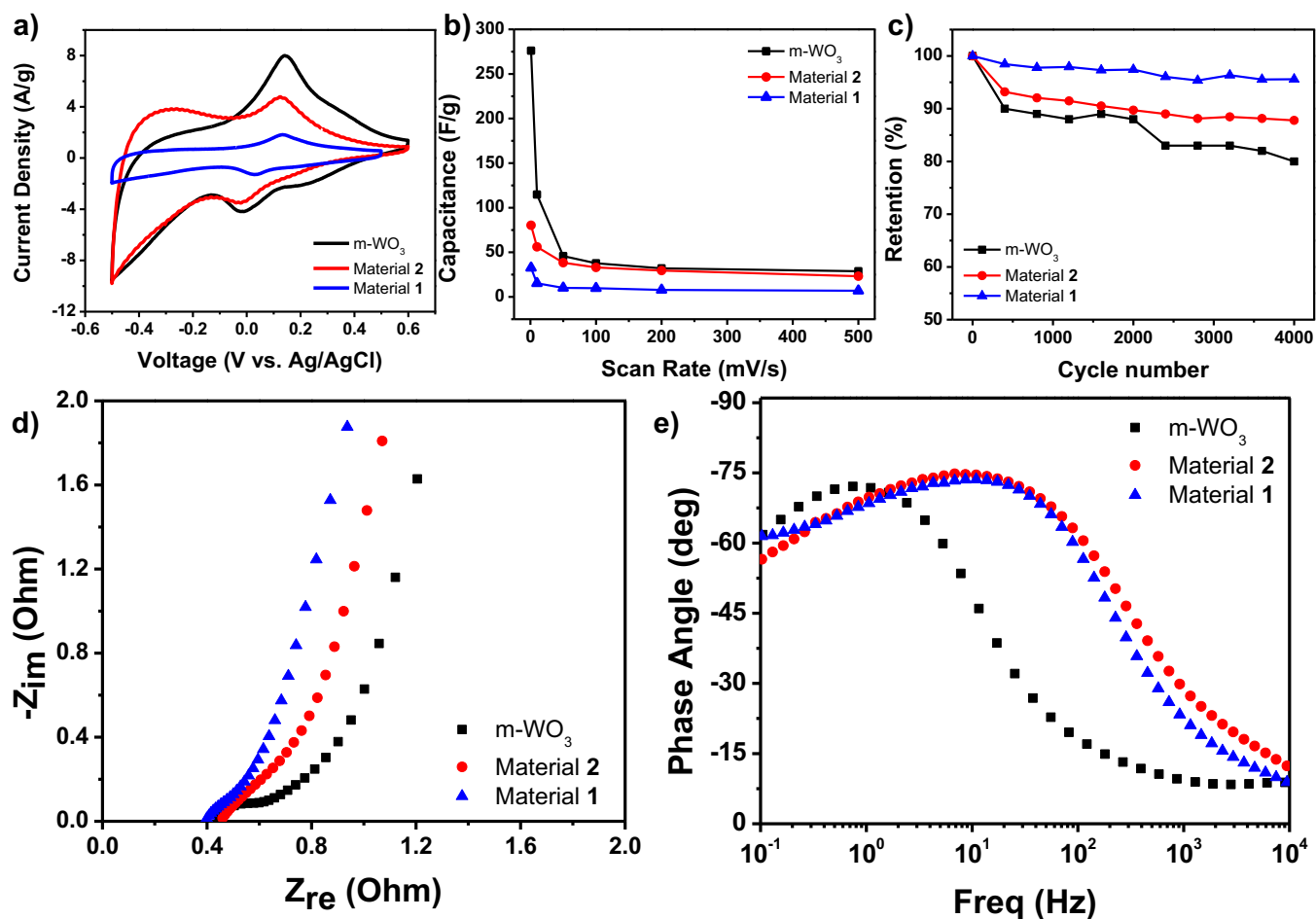
Fig. 4 Electrochemical properties of material **1**, **2**, and monoclinic WO_3 (m-WO_3). (a) cyclic voltammograms at a scan rate of 100 mV/s, (b) specific capacitance as a function of scan rates (c) cycling performance, (d) Nyquist and (e) Bode plots of material **1**, **2**, and m-WO_3 control.
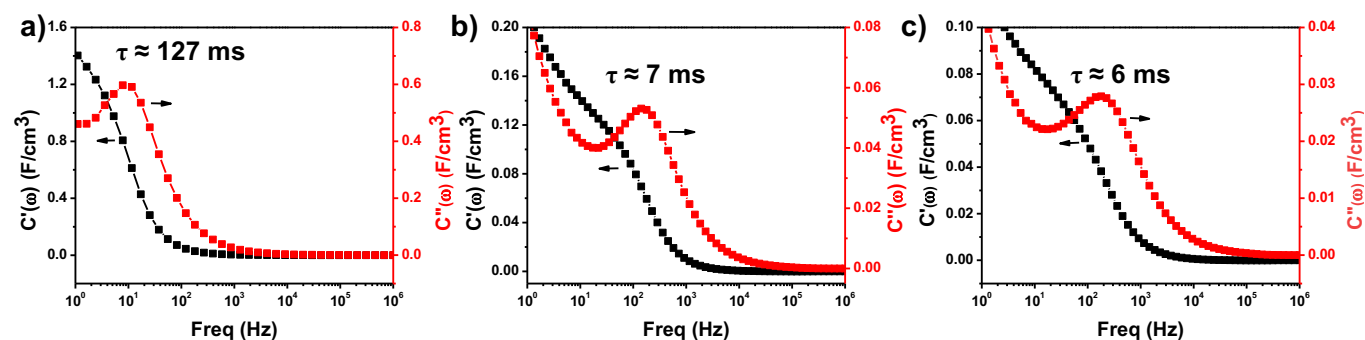
Fig. 5 Real, C'(ω), and imaginary, C''(ω), capacitance as a function of frequency with relaxation times for (a) m-WO₃, (b) material **1** and (c) material **2**.

and 81 F/g, respectively (**Fig. 4b**). Although there is a large capacitance difference at slow scan rates, the capacitance of material **2** and m-WO₃ are similar at scan rates of 50 mV/s and greater. Additionally, m-WO₃ loses over 80% of its initial capacitance at a scan rate of 50 mV/s, whereas the loss in capacitance of material **1** and **2** exhibit lower rates of capacitance loss. We tentatively attribute the lower capacitance values of material **1** and **2** to the lower effective surface area available to the electrolyte (**Fig. S13**).

Due to constant redox reactions, the structure of the metal oxide can become strained, leading to structural distortions during the charge-discharge process. This can cause cracking of the electrode over time, leading to a poor cycle life.[41] Therefore, the development of metal oxide-based materials that possess high thermal and chemical stability, which eventually affect the cycling stability would be necessary for the practical use of metal oxides as supercapacitor electrodes. To investigate long-term stability, all three materials were charged and discharged 4,000 times at a current density of 5 A/g. While the pristine m-WO₃ only preserved 80% of its initial capacitance, material **1** and material **2** proved to have higher stability with material **2** preserving 88% of its initial capacity and material **1** preserving 96% of its initial capacity (**Fig. 4c**). Due to the extensive cross-linking present in materials **1** and **2**, we speculate that the molecular cross-linker **I** may act as a mechanical support to WO₃, preventing structural degradation over time.

Another consequence of the low conductivity in most metal oxides is that both the charge transfer resistance and sheet resistance of the electrode are relatively high. Electrical impedence spectroscopy was used to investigate the resistive properties of the materials. In the Nyqiust plot, both materials **1** and **2** show a significant decrease in charge transfer resistance compared to pristine m-WO₃ (**Fig. 4d**). Additionally, in the lower frequency regions, the slope of materials **1** and **2** are steeper, indicating less diffusion resistance. From the Bode plot, the minimum phase angle is approximately -75° for all three samples, however, there is a large shift to higher frequencies for the cross-linked materials indicating a faster relaxation time (**Fig. 4e**). The relaxation time is an important factor of merit, indicating when a material transitions from resistive to capacitive behavior and is the time required to deliver the stored energy and power efficiently.[42] To determine the relaxation time of all three materials, we modeled the real, C'(ω), and imaginary, C''(ω), capacitance as a function of

frequency (**Fig. 5**).[28] A remarkable decrease in the response time for both materials **1** and **2** was observed. Pristine m-WO₃ shows a relaxation time of 127 ms, whereas materials **1** and **2** have a relaxation time of 7 ms and 6 ms, respectively. We attribute these results to the increase in conductivity due to the cross-linking present in materials **1** and **2**. Previous reports have shown that the molecular cross-linker, **I**, has remarkable kinetic stability and displays pseudometallic behavior due to extensive electron delocalization.[43-45]

In order to determine the possible electrocatalytic properties of material **1**, we studied its electron-transfer capability by using the ferri/ferrocene redox couple (**Fig. S14**). The peak-to-peak separation of material **1** is smaller than pristine m-WO₃, leading to a 21% increase in the observed electron-transfer-rate constant, k^0, with a value of 1.64 x 10^{-3} cm s^{-1}. The oxidation peak observed at 0.8 V can be attributed to the formation of the radical species $[B_{12}(OH)_{12}]^{1-}$.[46]

Conclusions

In summary, we have demonstrated a successful synthesis of a boron-rich hybrid tungsten oxide material and its utilization as a supercapacitor electrode with superior cycling stability to pristine tungsten oxide. The comprehensive structural study of material **1** revealed the formation of a cross-linked network of tungsten oxide nanoparticles with intact molecular boron-rich clusters. Importantly, the incorporation of the robust molecular cross-linker, **I**, into the network of tungsten oxide effectively preserved the specific capacitance of the material up to 4000 cycles and reduce the charge transfer resistance as well as the response time in comparison to that of pristine m-WO₃. Further improvements such as increasing the effective surface area could allow for capacitance values mirroring pristine m-WO₃, while retaining the benefits of incorporating **I**. These results highlight the promising capability of **I** in the hybrid metal oxide materials to ultimately obtain fast and stable metal oxide-based supercapacitors with high capacitances. This work further highlights the potential promise of boron cluster-containing materials as unique building blocks for the next generation of energy storage and conversion materials and devices.[47-65]

Conflicts of interest

Notes and references

1   P. Simon and Y. Gogotsi, *Nat. Mater.*, 2008, **7**, 845–854.
2   A. Noori, M. F. El-Kady, M. S. Rahmanifar, R. B. Kaner and M. F. Mousavi, *Chem. Soc. Rev.*, 2019, **48**, 1272–1341.
3   C. Y. Foo, A. Sumboja, D. J. H. Tan, J. Wang and P. S. Lee, *Adv. Energy Mater.*, 2014, **4**, 1400236.
4   J. Ji, L. L. Zhang, H. Ji, Y. Li, X. Zhao, X. Bai, X. Fan, F. Zhang and R. S. Ruoff, Nanoporous Ni(OH)2 *ACS Nano* 2013, **7**, 6237–6243.
5   M. Li, M. F. El-Kady, J. Y. Hwang, M. D. Kowal, K. March, H. Wang, Z. Zhao and R. B. Kaner, *Nano Research*, 2018, **11**, 2836–2846.
6   L. Y. Chen, Y. Hou, J. L. Kang, A. Hirata, T. Fujita and M. W. Chen, *Adv. Energy Mater.*, 2013, **3**, 851–856.
7   M. F. El-Kady, M. Ihns, M. Li, J. Y. Hwang, M. F. Mousavi, L. Chaney, A. T. Lech and R. B. Kaner, *PNAS*, 2015, **112**, 4233–4238.
8   A. K. Nayak, A. K. Das and D. Pradhan, *ACS Sustain. Chem. Eng.*, 2017, **5**, 10128–10138.
9   C. Liu, F. Li, M. Lai-Peng and H. M. Cheng, *Advanced Materials.*, 2010, **22**, E28–E62.
10 F. Zheng, C. Xi, J. Xu, Y. Yu, W. Yang, P. Hu, Y. Li, Q. Zhen, S. Bashir and J. L. Liu, *J. Alloys Compd.*, 2019, **772**, 933–942.
11 X. Liu, G. Sheng, M. Zhong and X. Zhou, *Nanoscale*, 2018, **10**, 4209–4217.
12 M. Qiu, P. Sun, L. Shen, K. Wang, S. Song, X. Yu, S. Tan, C. Zhao and W. Mai, *J. Mater. Chem. A*, 2016, **4**, 7266–7273.
13 L. Hu, W. Chen, X. Xie, N. Liu, Y. Yang, H. Wu, Y. Yao, M. Pasta, H. N. Alshareef and Y. Cui, *ACS Nano*, 2011, **5**, 8904–8913.
14 J. Y. Hwang, M. F. El-Kady, Y. Wang, L. Wang, Y. Shao, K. Marsh, J. M. Ko and R. B. Kaner, *Nano Energy*, 2015, **18**, 57–70.
15 Y. H. Lin, T. Y. Wei, H. C. Chien and S. Y. Lu, *Adv. Energy Mater.*, 2011, **1**, 901–907.
16 Y. Zhu, X. Ji, C. Pan, Q. Sun, W. Song, L. Fang, Q. Chen and C. E. Banks, *Energy Environ. Sci.,* 2013, **6**, 3665–3675.
17 H. Wei, X. Yan, S. Wu, Z. Luo, S. Wei and Z. Guo, *J. Phys. Chem. C*, 2012, **116**, 25052–25064.
18 D. Jung, L. M. A. Saleh, Z. J. Berkson, M. F. El-Kady, J. Y. Hwang, N. Mohamed, A. I. Wixtrom, E. Titarenko, Y. Shao, K. McCarthy, J. Guo, I. B. Martini, S. Kraemer, E. C. Wegener, P. Saint-Cricq, B. Ruehle, R. R. Langeslay, M. Delferro, J. L. Brosmer, C. H. Hendon, M. Gallagher-Jones, J. Rodriguez, K. W. Chapman, J. T. Miller, X. Duan, R. B. Kaner, J. I. Zink, B. F. Chmelka and A. M. Spokoyny, *Nat. Mater.*, 2018, **17**, 341–348.
19 A. E. Danks, S. R. Hall and Z. Schnepp, *Mater. Horiz.*, 2016, **3**, 91–112.
20 I. Salzmann and G. Heimel, *J. Electron Spectrosc. Relat. Phenom.*, 2015, **204**, 208–222.
21 D. Jung, F. Raffan-Montoya, R. Ramachandran, Y. Zhang, T. Islamoglu, G. Marin, E. A. Qian, R. M. Dziedzic, O. K. Farha, S.

I. Stoliarov and A. M. Spokoyny, *Chem. Commun.*, 2019, **55**, 8852–8855.
22 J. L. Barton, A. I. Wixtrom, J. A. Kowalski, E. A. Qian, D. Jung, F. R. Brushett and A. M. Spokoyny, *ACS Appl. Energy Mater.*, 2019, **2**, 4907–4913.
23 R. Ramachandran, D. Jung and A. M. Spokoyny, *NPG Asia Mater.*, 2019, *11*:19.
24 A. I. Wixtrom, Y. Shao, D. Jung, C. W. Machan, S. N. Kevork, E. A. Qian, J. C. Axtell, S. I. Khan, C. P. Kubiak and A. M. Spokoyny, *Inorg. Chem. Front.*, 2016, **3**, 711–717.
25 C. Jaeger and F. Hemmann, *Solid State Nucl. Mag.*, 2014, **57**, 22–28.
26 J. Moldenhauer, M. Meier and D. W. Paul, *J. Electrochem. Soc*, 2016, **163**, H672–H678.
27 S. J. Konopka and M. Bruce, *Anal. Chem.* 1970, **42**, 1741–1746.
28 P. L. Taberna, P. Simon and J. F. Fauvarque, *J. Electrochem. Soc.*, 2003, **150**, A292–A300.
29 O. K. Farha, R.L. Julius, M. W. Lee, R. E. Huertas, C. B. Knobler and M. F. Hawthorne, *J. Am. Chem. Soc.*, 2005, **127**, 18243–18251.
30 M. S. Messina, J. C. Axtell, Y. Wang, P. Chong, A. I. Wixtrom, K. O. Kirlikovali, B. M. Upton, B. M. Hunter, O. S. Shafaat, S. I. Khan, J. R. Winkler, H. B. Gray, A. N. Alexandrova, H. D. Maynard and A. M. Spokoyny, *J. Am. Chem. Soc.*, 2016, **138**, 6952–6955.
31 E. A. Qian, A. I. Wixtrom, J. C. Axtell, A. Saebi, D. Jung, P. Rehak, Y. Han, E. H. Moully, D. Mosallaei, S. Chow, M. S. Messina, J. Y. Wang, A. T. Royappa, A. L. Rheingold, H. D. Maynard, P. Král and A. M. Spokoyny, *Nat. Chem.,* 2017, **9**, 333–340.
32 A. Jain, S. P. Ong, G. Hautier, W. Chen, W.D. Richards, S. Dacek, S. Cholia, D. Gunter, D. Skinner, G. Ceder and K.A. Persson, *APL Materias*, 2013, **1**, 011002.
33 N. L. Houx, G. Pourroy, F. Camerel, M. Comet and D. Spitzer, *J. Phys. Chem. C*, 2010, **114**, 155–161.
34 C. Chacón, M. Rodríguez-Pérez, G. Oskam and G. Rodríguez-Gattorno, *J. Mater. Sci: Mater Electron*, 2015, **26**, 5526–5531.
35 N. Sharma, M. Deepa, P. Varshney and S. A. Agnihotry, *Thin Solid Films*, 2001, **401**, 45–51.
36 T. G. G. Maffeis, D. Yung, L. LePennec, M. W. Penny, R. J. Cobley, E. Comini, G. Sberveglieri and S. P. Wilks, *Surf. Sci.*, 2007, **601**, 4953–4957.
37 N. Feng, A. Zheng, Q. Wang, P. Ren, X. Gao, S.-B. Liu, Z. Shen, T. Chen and F. Deng, *J. Phys. Chem. C*, 2011, **115**, 2709–2719.
38 V. Lokhande, A. Lokhande, G. Namkoong, J. H. Kim and T. Ji, *Results Phys.*, 2019, **12**, 2012–2020.
39 W. Sun, M. T. Yeung, A. T. Lech, C. W. Lin, C. Lee, T. Li, X. Duan, J. Zhou and R. B. Kaner, *Nano Lett.*, 2015, **15**, 4834–4838.
40 S. Cong, Y. Tian, Q. Li, Z. Zhao and F. Geng, *Adv. Mater.*, 2014, **26**, 4260–4267.
41 M. Zhi, C. Xiang, J. Li, M. Li and N. Wu, *Nanoscale*, 2013, **5**, 72–88.
42 C. Portet, G. Yushin and Y. Gogotsi, *Carbon*, 2007, **45**, 2511–2518.
43 M. W. Lee, O. K. Farha, M. F. Hawthorne and C. H. Hansch, *Angew. Chem. Int. Ed.*, 2007, **46**, 3018–3022.
44 A. R. Pitochelli and M. F. Hawthorne, *J. Am. Chem. Soc.*, 1960, **82**, 3228–3229.
45 R. Hoffmann and W. N. Lipscomb, *J. Chem. Phys.*, 1962, **36**, 2179–2189.
46 N. Van, I. Tiritiris, R. F. Winter, B. Sarkar, P. Singh, C. Duboc, A. Muñoz-Castro, R. Arratia-Pérez, W. Kaim and T. Schleid, *Chem. Eur. J.,* 2010, **16**, 11242–11245.
47 L. Cerdán, J. Braborec, I. Garcia-Moreno, A. Costela and M. G. S. Londesborough, *Nat Commun.*, 2015, **6**, 5958
48 J. A. Teprovich Jr., H. Colón-Mercado, A. L. Washington II, P. A. Ward, S. Greenway, D. M. Missimer, H. Hartman, J. Velten, J.

H. Christian and R. Zidan, *J. Mater. Chem. A*, 2015, **3**, 22853–22859.

49 R. Núñez, M. Tarrés, A. Ferrer-Ugalde, F. F. de Biani and F. Teixidor, *Chem. Rev.*, 2016, **116**, 14307–14378.

50 H. Naito, K. Nishino, Y. Morisaki, K. Tanaka and Y. Chujo, *J. Mater. Chem. C*, 2017, **5**, 10047–10054.

51 R. Ruiz-Rosas, I. Fuentes, C. Viñas, F. Teixidor, E. Morallón and D. Cazorla-Amorós, *Sustainable Energy Fuels*, 2018, **2**, 345–352.

52 C. −W. Kung, K. Otake, C. T. Buru, S. Goswami, Y. Cui, J. T. Hupp, A. M. Spokoyny and O. K. Farha, *J. Am. Chem. Soc.*, 2018, **140**, 3871–3875.

53 N. T. Hahn, T. J. Seguin, K. −C. Lau, C. Liao, B. J. Ingram, K. A. Persson and K. R. Zavadil, *J. Am. Chem. Soc.*, 2018, **140**, 35, 11076–11084.

54 M. Kar, O. Tutusaus, D. R. MacFarlane and R. Mohtadi, *Energy Environ. Sci.*, 2019, **12**, 566–571.

55 Y. Zhu, S. Gao and N. S. Hosmane, *Inorg. Chim. Acta*, 2018, **471**, 577–586.

56 S. P. Fisher, A. W. Tomich, S. O. Lovera, J. F. Kleinsasser, J. Guo, M. J. Asay, H. M. Nelson and V. Lavallo, *Chem. Rev.*, 2019, **119**, 8262–8290.

57 T. J. Aubry, J. C. Axtell, V. M. Basile, K. J. Winchell, J. R. Lindemuth, T. M. Porter, J. −Y. Liu, A. N. Alexandrova, C. P. Kubiak, S. H. Tolber, A. M. Spokoyny and B. J. Schwartz, *Adv. Mater.*, 2019, **31**, 1805647.

58 Z. Peng, K. Zhang, Z. Huang, Z. Wang, S. Duttwyler, Y. Wang and P. Lu, *J. Mater. Chem. C*, 2019, **7**, 2430–2435.

59 K. Zhang, Y. Shen, X. Yang, J. Liu, T. Jiang, N. Finney, B. Spingler and S. Duttwyler, *Chem. Eur. J.*, 2019, **25**, 8754–8759.

60 I. Fuentes, M. J. Mostazo-Ljpez, Z. Kelemen, V. Compañ, A. Andrio, E. Moralljn, D. Cazorla-Amorjs, C. Viñas and F. Teixidor, *Chem. Eur. J.*, 2019, **25**, 14308–14319.

61 M. Jørgensen, P. T. Shea, A. W. Tomich, J. B. Varley, M. Bercx, S. Lovera, R. Černý, W. Zhou, T. J. Udovic, V. Lavallo, T. R. Jensen, B. C. Wood and V. Stavila, *Chem. Mater.*, 2020, **32**, 1475–1487.

62 M. Jørgensen, S. R. H. Jensen, T. D. Humphries, M. R. Rowles, M. V. Sofianos, C. E. Buckley, T. R. Jensen and M. Paskevicius, *J. Phys. Chem. C*, 2020, doi: 10.1021/acs.jpcc.0c02523;

63 Z. Li, C. Ma, Y. Wen, Z. Wei, X. Xing, J. Chu, C. Yu, K. Wang and Z. −K. Wang, Nano Research, 2020, **13**, 196–202.

64 K. P. Anderson, M. A. Waddington, G. J. Balaich, J. M. Stauber, N. A. Bernier, J. R. Caram, R. I. Djurovich and A. M. Spokoyny, *Dalton Trans.*, 2020 doi:10.1039/d0dt00826e

65 M. Keener, C. Hunt, T. G. Carroll, V. Kampel, R. Dobrovetsky, T. W. Hayton and G. Ménard, *Nature*, 2020, **577**, 652–655.

ARTICLE

Table of Contents
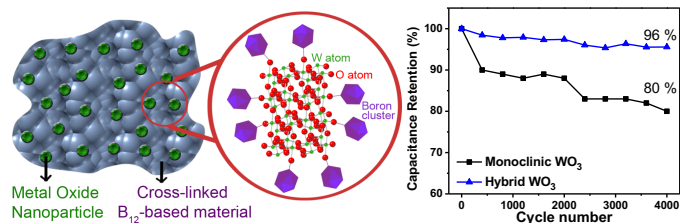
A Boron-rich hybrid tungsten oxide material with enhanced cycling stability up to 4000 cycles compared to that of pristine tungsten oxide